



**HAL**  
open science

# An experimental investigation of galling phenomenon generated in an alternated sliding ring-on-ring interface: Application to a full-scale solid lubricant interface

Pauline Faura, Siegfried Fouvry, Pauline Ronfard, Nabil Marouf, Thibault Mathon

## ► To cite this version:

Pauline Faura, Siegfried Fouvry, Pauline Ronfard, Nabil Marouf, Thibault Mathon. An experimental investigation of galling phenomenon generated in an alternated sliding ring-on-ring interface: Application to a full-scale solid lubricant interface. *Wear*, 2022, 508-509, pp.204457. 10.1016/j.wear.2022.204457 . hal-03766176

**HAL Id: hal-03766176**

**<https://hal.science/hal-03766176>**

Submitted on 31 Aug 2022

**HAL** is a multi-disciplinary open access archive for the deposit and dissemination of scientific research documents, whether they are published or not. The documents may come from teaching and research institutions in France or abroad, or from public or private research centers.

L'archive ouverte pluridisciplinaire **HAL**, est destinée au dépôt et à la diffusion de documents scientifiques de niveau recherche, publiés ou non, émanant des établissements d'enseignement et de recherche français ou étrangers, des laboratoires publics ou privés.

# An experimental investigation of galling phenomenon generated in an alternated sliding ring-on-ring interface: Application to a full-scale solid lubricant interface

Pauline Faura<sup>1,2)\*</sup>, Siegfried Fouvry<sup>1)\*</sup>, Pauline Ronfard<sup>2)</sup>, Nabil Marouf<sup>2)</sup>, Thibault Mathon<sup>2)</sup>

<sup>1)</sup>LTDS, Ecole Centrale de Lyon, Ecully, France

<sup>2)</sup>Vallourec Research Center, Aulnoye-Aymeries, France

\*Corresponding authors: [pauline.faura@ec-lyon.fr](mailto:pauline.faura@ec-lyon.fr); [siegfried.fouvry@ec-lyon.fr](mailto:siegfried.fouvry@ec-lyon.fr)

## Abstract

A fully instrumented ring-on-ring galling test has been developed based on the ASTM G196 test principle. Torque records allow computation of the coefficient of friction and other tribological parameters to capture wear behavior of the interface. Contact electrical resistance is also recorded helping to detect galling onset in the contact. A solid lubricant anti-galling solution in OCTG connections involving a coated versus steel interface has been studied. Tests have been stopped at different sliding distances to perform surface analysis and characterize wear mode and severity. Wear scars have been expertized using optical, SEM, EDS, surface and  $\mu$ -hardness profile analysis such that the degradation scenario of the coating and the steel surface can be drawn up. Moreover, an analysis in terms of friction coefficient can be developed describing the evolution from pure lubricated interface to fully galled interface.

## 1. Introduction

Steel tubing is implied in for fluid transport of oil and gas industries [1]. As some pipes need to go in deep wells, tubes are screwed to each other in order to build the pipe string from the surface. Strings endure many different solicitations during both installation and production phases [2]. It is important that all the parts of the string resist these solicitations while ensuring sealability. Tubes are assembled in two steps: a screwdriving phase and a tightening phase where the metal-to-metal (MTM) junction of the connection is put in contact and a tightening torque is applied. It is important to generate high contact at the MTM zone to ensure the sealing of the junction [3]. During installation and for maintenance reasons, the tubes need to be disassembled and assembled several times. These repetitive movements under high pressure, referred to as reciprocating sliding, are responsible of wear at the zones in contact in the form of galling (Figure 1).

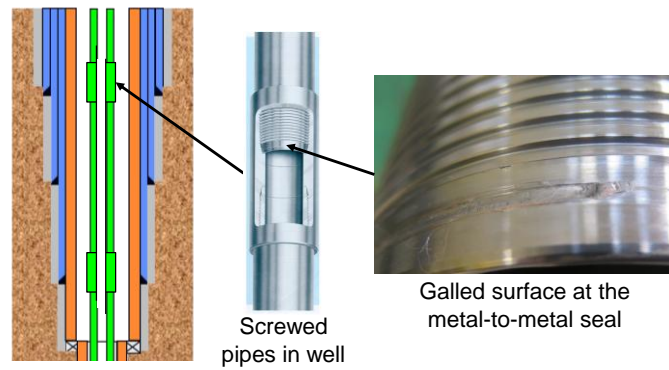


Figure 1 Illustration of galling phenomenon in screw assembly of steel tubing pipes

Wear rate and mechanisms are influenced by lots of parameters such as contact pressure, frequency or contact geometry. Former studies have shown that adhesive wear and galling phenomenon are highly influenced by the loading conditions namely the contact pressure  $p$  and the sliding speed  $v$  or more concisely the so-called “ $p \cdot v$ ” factor [4]. Investigations around this product revealed that a  $p \cdot v$  threshold can be found indicating the transition between abrasion and adhesion or between “mild” and “severe” wear [5]. One of the parameters strongly affecting the wear rate as well as the mechanism is the contact geometry [6,7]. In the case of non-conforming contact (i.e. small contact surface), high wear rate is observed, and damage occurs primarily by oxidative-abrasive wear whereas adhesion prevails in conforming contact. The activation of adhesive wear phenomenon was indeed addressed considering the contact oxygenation concept (COC) [8]. As oxygen penetrates the contact, oxidation occurs limiting adhesion between the bulk materials. In conforming contact, the interface oxygenation is rather low leading to a so-called “oxygen-deprived zone” in the center of the contact where seizure and material transfers are promoted. Under high contact pressure, oxygenation at the center is also very limited so large adhesion zones can be observed even for small contacts. Juoksukangas [9] shows that annular flat-on-flat contact creates local adhesion spots which revealed significant cracking and plastic deformation. This can be explained by local stress concentration appearing around the adhesion spot at least once in the loading history. Arnaud et al [10], combining local surfaces wear, COC and third body effects, simulated such phenomena for a Ti-6Al-4V fretting cylinder-on-flat contact. They demonstrated that the partition between the inner adhesive and the surrounding abrasive wear domains may induce contact overpressures at the boundary between these domains which in turn favors cracking phenomenon.

Hence, many investigations suggested that galling (i.e. adhesion processes) appears with high contact pressure and/or high sliding speed, in other words, with high  $p \cdot v$  factor conditions. It was concluded that when the Archard’s power density  $\omega = p \cdot v$  exceeds a threshold  $\omega_{th}$  value, galling mechanism is activated. This approach was extended using an equivalent friction power density  $\phi$  to formalize the seizure endurance of solid lubricants subjected to fretting sliding in [11]. Hence, when  $\omega$  exceeds a given  $\omega_{th}$ , the protective layer (coatings or native oxide layer) is eliminated by interfacial shear strains. Small welded bonds

form between the bulk materials in contact and are then ripped off as sliding continues. This destruction causes a significant increase of the friction coefficient inducing a complete seizure on the mechanical connection.

Galling, defined as a surface damage arising between surface sliding solids distinguished by macroscopic, usually localized, roughening and creation of protrusions above the original surface [12], is still misunderstood. It may involve non-uniform material transfer and/or plastic flow on both macroscopic and microscopic scales [13]. Authors agreed that galling can be related to adhesive wear phenomenon and therefore can be formalized using the  $\omega = p \cdot v$  factor [14].

Cross-section observations of galling spots underlined a plastically deformed layer (general deformation layer, GDL), a third body layer (TBL) and, under certain conditions, an extremely hard plastically deformed layer above the bulk material known as TTS layer (Tribologically Transformed Structure) [15]. To measure the galling performance of the sliding interface, the ASTM G196-08 test procedure can be applied. As illustrated in Figure 2, the specimens consist in two concentric hollow cylinders with the mated ends. This results in annulus-shaped contact area. One specimen is rotated about its axis and the other is held fixed [12]. The results of the experimentations provide the rate of galling occurrences for the given loading conditions and allow a preliminary material ranking [16]. In OCTG field, a pin-and-box rig has been developed by Ertas et al. reproducing accurately the contact conditions found in a connection [17]. This test machine can be used to analyze friction behavior and galling resistance of different materials [18,19].

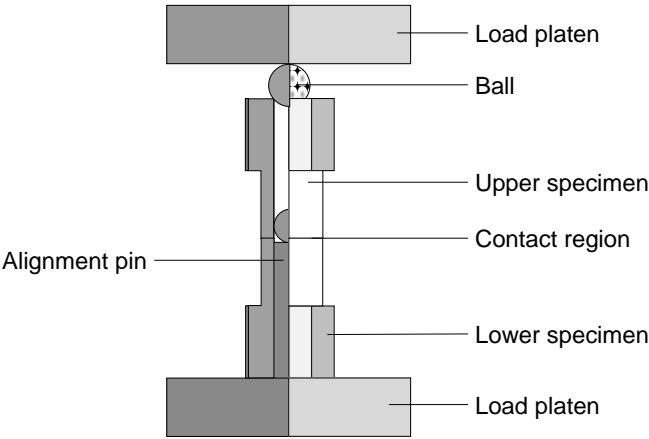


Figure 2 Schematic diagram of galling test method ASTM G196-08 [12]

One objective of this work is to develop an original galling test, reproducing the ASTM G 196-08 sliding conditions adapted for actual industrial tube connections focusing on galling appearance at MTM seal. The main interest of such macro galling test is the opportunity to test industrial surfaces considering the real microstructure and surface manufacturing process. A second objective of this work is to detail the damage scenario inducing the incipient galling phenomenon by combining online friction and electrical contact resistance

analysis. A simple phenomenological modelling is finally induced to formalize the friction behavior of an “anti-galling” solid lubricant coating.

2. Experimental set-up

2.1. Studied interface

Figure 3 illustrated the studied interface. The bulk specimens are made of carbon steel with a composition detailed in Table 1. A specific heat treatment including a water quench followed by a tempering treatment is applied leading to a 550 MPa yield strength [20].

Table 1 Steel composition (mass fraction)

	C	Mn	Ni	Cu	P	S	Si
% max	0.43	1.90	0.25	0.35	0.030	0.030	0.45

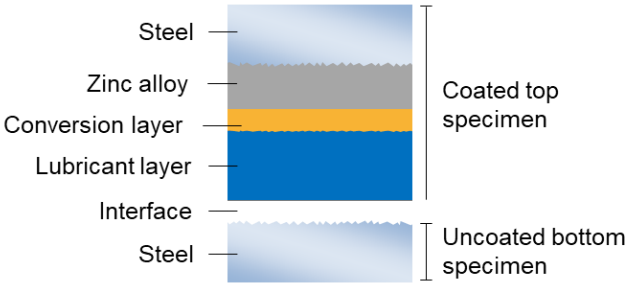


Figure 3 Illustration of the fretted interface, top sample is coated with a multilayer coating (sandblasting, zinc alloy, conversion layer and lubricant polymer layer), bottom sample has no surface treatment

Figure 4 illustrates the microstructure as well as the micro-hardness profile of the studied steel counterparts. The bottom sample surface is “as machined”, no surface treatment or coating is applied. The upper sample is sandblasted, plated with zinc alloy, and coated with a lubricating polymer. Figure 3 illustrates the multilayer coating structure of the upper specimens.

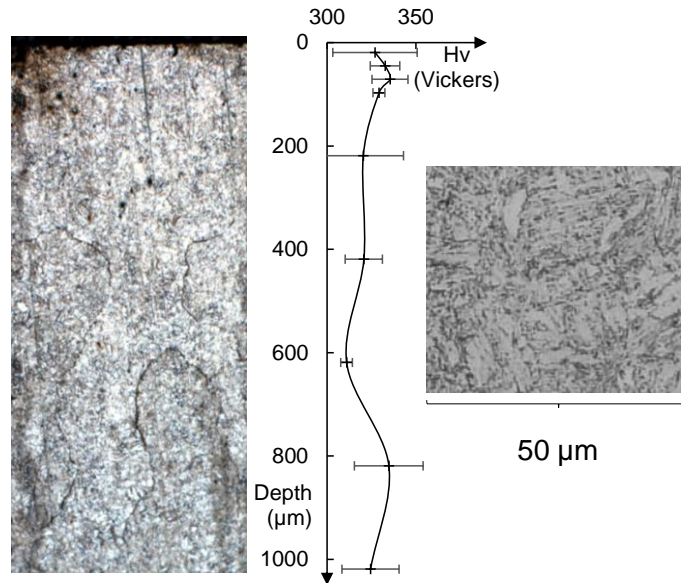


Figure 4 Illustration of the studied steel (similar for both counterfaces)

## 2.2. Specimen geometry

As mentioned previously, the steel specimens are directly machined from real tube. They consist in tubular shape designs depicted in Figure 5.

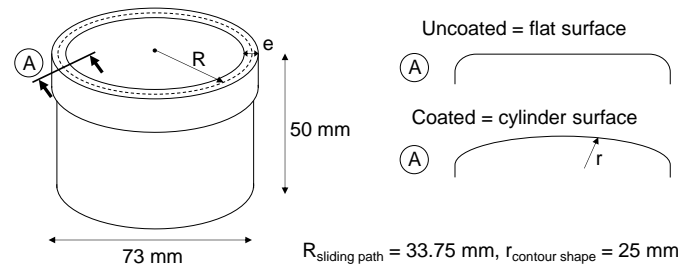


Figure 5 Illustration of the studied contact geometry

The “as machined” uncoated bottom surface is flat whereas the coated surface displays a half-torus shape with  $r_c = 25$  mm curvature radius. The surface roughness of “as machined” steel specimen is about  $R_a = 1.2 \mu\text{m}$ . As in “pin-and-box” tests, the shape of the specimens has been defined to represent MTM seal geometry (often a “cylinder-on-flat” contact) [17]. It has been decided that surfaces in contact are orthogonal to the cylinder axis to allow a good control of sliding conditions and contact pressure. Fine surface analyses are also facilitated.

## 2.3. Test machine

Figure 6 illustrates the experimental set up. It consists in a 250 kN – 2200 N·m MTS Axial-torsion hydraulic frame in which a dedicated self-aligning ring-on-ring rotating sliding apparatus so-called TGT (i.e. Tubular Galling Test) is implemented.

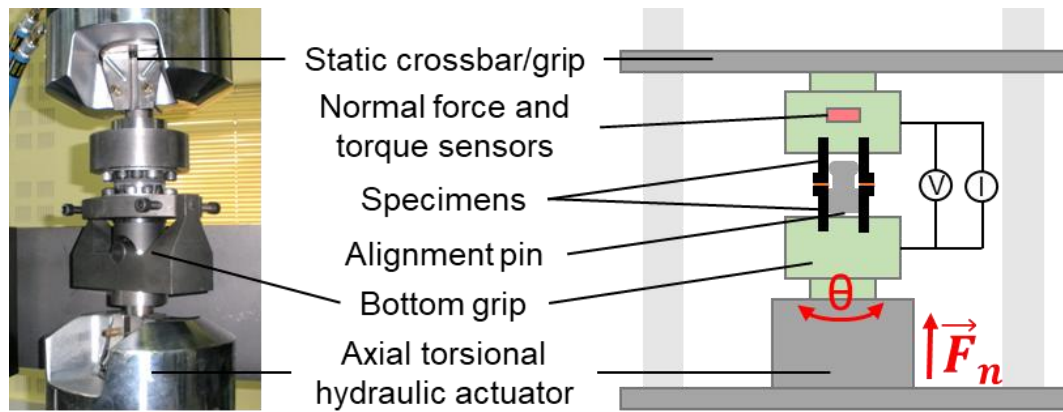


Figure 6 Illustration of the test machine used for the given galling analysis

The principle of this test is equivalent to the ASTM G196-08 norm except that the dimension of the specimens and the loading capacity were increased to investigate real contact size. Both the upper and the lower specimen holders are connected via hydraulic grips to the loading frame. Normal force  $F_n$  and torque  $T$  are measured by a load cell located on the upper crossbar whereas the normal force and the alternating rotation are applied by the bottom hydraulic actuator. The test system was designed to support a normal load from 10 to 180 kN assuming that the torque remains below 2000 N.m. The angular displacement can be applied from  $\pm 0.5^\circ$  to  $\pm 45^\circ$  which, for the given  $R_{\text{sliding path}} = 33.75$  mm, leads to a linear sliding amplitude between  $\pm 0.3$  mm and  $\pm 26$  mm. The maximum frequency is about 10 Hz for  $\theta = \pm 45^\circ$ . Figure 7 illustrates a typical wear scar generated by such alternated ring-on-ring test system (i.e. TGT). The apparatus is inserted in an ambient chamber allowing the control of the relative humidity from 5 to 80% and the temperature from 10 to 80°C. The given investigation was done for ambient dry conditions. However, the test can be adapted to work in liquids and potentially wider cryogenic or high temperature conditions.

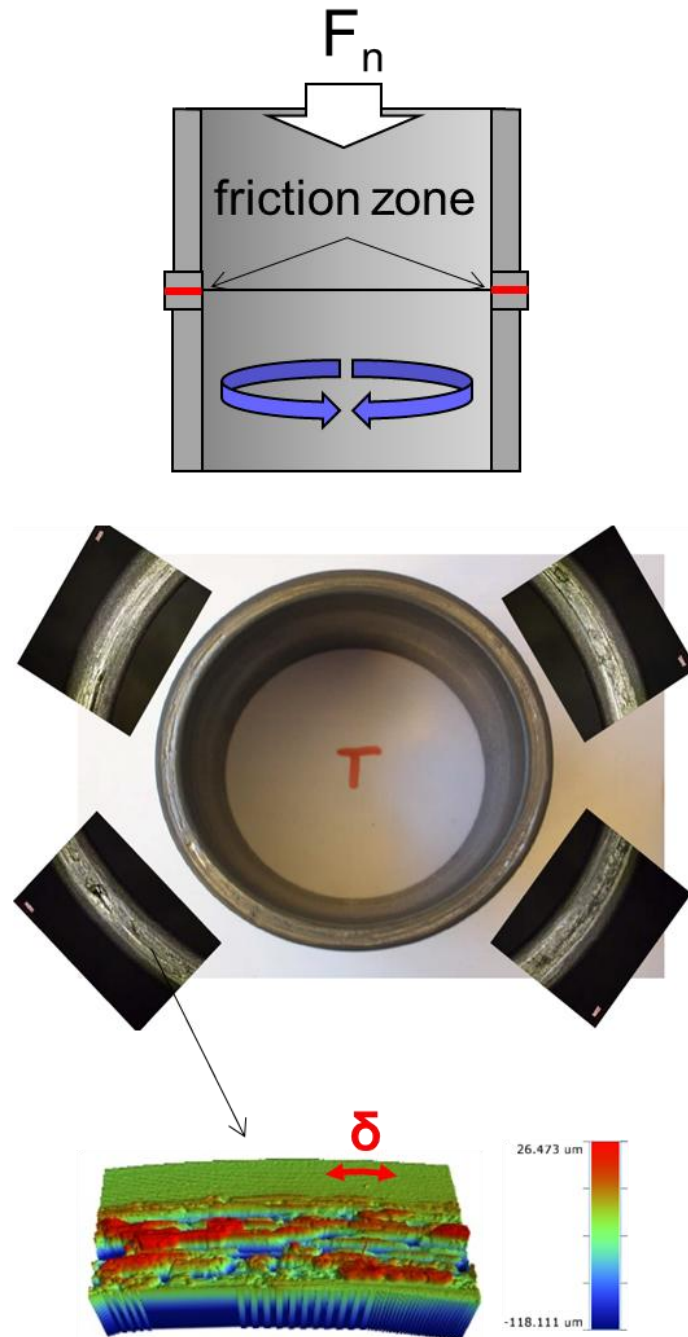


Figure 7 Illustration of the wear scar observed on the “as-machined” specimen generated by the TGT system (studied as machined/coated interface,  $F_n = 40 \text{ kN}$ ,  $f = 0.2 \text{ Hz}$ ,  $\theta^* = \pm 25^\circ$ ,  $D = \pm 15 \text{ vmm}$ )

#### 2.4. Test condition

The loading conditions are kept constant with  $F_n = 40 \text{ kN}$ ,  $\theta = \pm 25^\circ$ ,  $D = \pm 15 \text{ mm}$  and  $f = 0.2 \text{ Hz}$ . Sliding conditions have been defined after pressure and sliding speed levels applied at MTM seal during the make-up of the connection [21]. Alternating rotation allows to achieve high sliding distances necessary to observe galling appearance of lubricated interface. The test temperature was adjusted around  $25^\circ\text{C}$  and the relative humidity around



30%. Considering the contact perimeter  $\phi = 2\pi R = 212$  mm, it leads to a linear normal force of  $F_{nL} = 189$  N/mm. Considering the Hertzian theory for cylinder-on-flat interface such that:

$$a_H = \left( \frac{4 \cdot F_{nL} \cdot r_c}{\pi \cdot E^*} \right)^{\frac{1}{2}} \quad (1)$$

$$\text{and } P_{max} = \frac{2 \cdot P}{\pi \cdot a_H} = \left( \frac{F_{nL} \cdot E^*}{\pi \cdot r_c} \right)^{\frac{1}{2}} \quad (2)$$

$$\text{with } E^* = \frac{E}{2 \cdot (1-\nu)} \quad (3)$$

We get a  $p_{max} = 560$  MPa and  $a_H = 0.28$  mm with  $E = 210 \cdot 10^9$  Pa,  $\nu = 0.3$  and  $r_c = 25$  mm. Figure 8 illustrates the contact configuration. A Fuji film© pressure paper was used to verify the good alignment of the contact surface before test. A homogeneous distribution of linear normal force is observed confirming the relevance of the self-aligning capacity of the given TGT system.

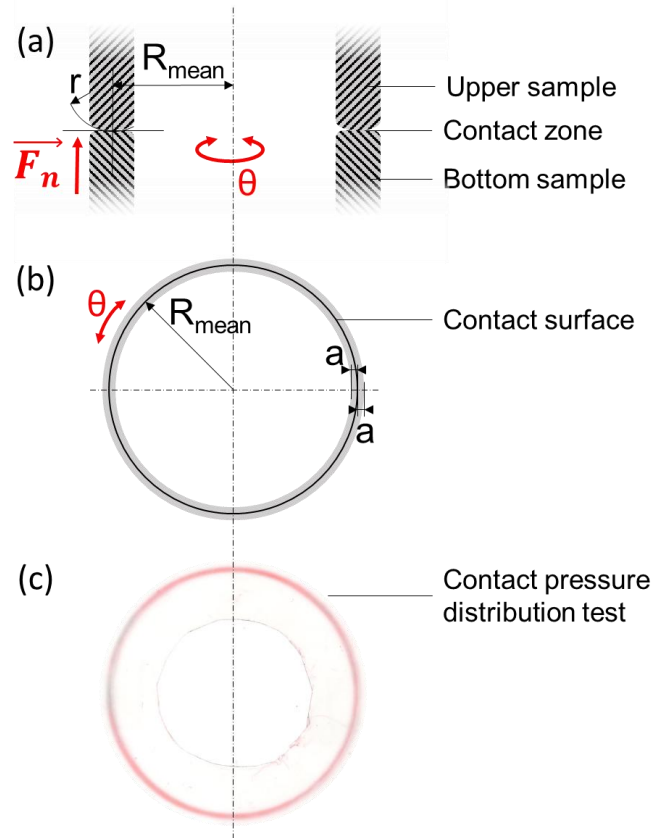


Figure 8 Scheme of the contact geometry (not to scale): (a) cross-section view, (b) top view, (c) contact pressure distribution test with Fuji film paper

## 2.5. Test instrumentation

The TGT is instrumented to achieve online monitoring of the surface damage. The torque values (T) allowing to compute the tangential force  $F_t$  (i.e.  $F_t = T/R$ ) and displacement (i.e.  $\delta = R \cdot \theta$ ) allow to plot the  $F_t$ - $\delta$  sliding cycle (Figure 9).

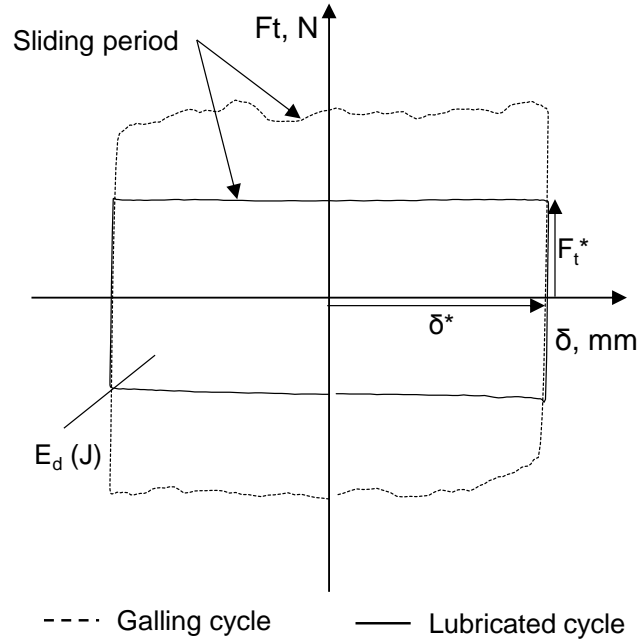


Figure 9 Illustration of a sliding cycle extracted from the TGT experiment

From this  $F_t$ - $\delta$  sliding cycle, we can extract the friction work (i.e. friction energy) ( $E_d$ ), the tangential force amplitude  $F_t^*$ , the tangential displacement amplitude ( $\delta^*$ ) as well as the effective sliding amplitude. This latter is estimated when the tangential force is zero so that no test apparatus accommodation is interfering with the contact displacement (i.e. the measured displacement is given by an LVDT sensor located next to the hydraulic actuator). To quantify the friction behavior, we consider the nominal friction parameter so that  $\mu = F_t^*/F_n$ .

Figure 9 compares two sliding cycles under lubricated and galling situations. The galling damage is characterized by a higher friction response and a more disturbed evolution of the friction force during the sliding plateau. Such friction fluctuations appear as an interesting indicator to detect the incipient galling process. To quantify this friction perturbation, an equivalent mean parameter, commonly applied to quantify surface roughness (i.e. Ra surface roughness average), is applied to formalize the so-called “friction noise” ( $\mu^*$ ) of the sliding period.

$$\mu^* = \frac{1}{t_f - t_i} \int_{t_i}^{t_f} \frac{|F_t(t) - F_{t, mean}|}{F_n} dt \quad (4)$$

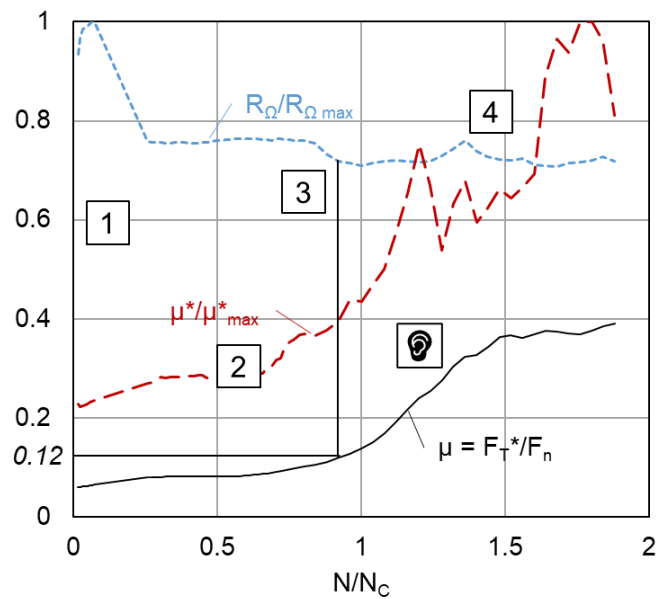
where  $t_i$  corresponds to the beginning of the sliding plateau and  $t_f$  stands for the end of the sliding plateau before the reversal.

In addition to the friction analysis, the interface electrical resistance is also measured using a four-point method previously detailed in Figure 6. The current was set at 5 mA while the voltage is measured using a dedicated analogical amplifier, it was possible to detect contact resistance  $R_\Omega$  fluctuations below few milliohms. After the test, optical, SEM and EDS analysis were performed on the fretted surface as well as along the cross-section. 3D surface profiles

were also done to quantify the galling surface perturbations and Vickers hardness measurements were performed to quantify the subsurface cyclic plastic deformations.

### 3. Results

For confidential aspects, the test durations are normalized by a critical cycle  $N_c$ . This  $N_c$  is related to a discontinuity of the friction coefficient (COF) evolution when the solid lubricant is removed. Figure 10 illustrates the typical evolution of the sliding interface comparing the evolution of the COF ( $\mu$ ), the RMS noise of the sliding period and the ECR (Electrical Contact Resistance) evolution.




- 1  $\mu \approx 0,07$   
Resistivity drop - COF stabilization
- 2  $\mu \approx 0,1$   
First fluctuations of the cycle sliding plate rugosity before the COF raises
- 3  $\mu \approx 0,12$   
First fluctuations of the electrical resistance
- 4  $\mu \approx 0,3$   
Beginning of larger fluctuations on the cycle rugosity and electrical resistance
-   $\mu \approx 0,3$   
First audible acoustic emission

Figure 10 Evolution of the COF,  $\mu^*$  (normalized by  $\mu^*_{max}$ ) and  $R_\Omega$  (normalized by  $R_{\Omega_{max}}$ ) for a typical sliding test  $F_n = 40$  kN,  $f = 0.2$  Hz,  $\theta^* = \pm 25^\circ$ ,  $D = \pm 15$  mm)

After a short stabilization, the COF displays a progressive increase until a second plateau around  $\mu = 0.4$ . After this short plateau, the COF rises again until exceeding 0.6 value. Henceforth, the behavior of the recorded parameters can be linked to this COF evolution. Five events can be identified as illustrated in Figure 10. The friction noise  $\mu^*$  parameter displays a quite similar evolution as the friction variable  $\mu$ . It shows a stable evolution until

$\mu = 0.1$ , then displays a disturbed evolution just before the rising of  $\mu$ . It is interesting to note that, although the friction coefficient displays a continuous evolution, the  $\mu^*$  parameter allows, by the presence of fluctuation, to identify the first mechanisms of surface damage. Based on  $\mu^*$ , the first damage process seems to be observed for  $N/N_c = 1$  which also corresponds to the inflexion point of the friction coefficient rise. Regarding ECR behavior, a fast decreasing is observed at the beginning which can be attributed to local metal - metal interaction when the surface asperities pierce the top solid lubricating bond. Then, very stable evolution is observed until  $N/N_c = 1.2$  which corresponds to  $\mu = 0.12$ . After that, a disturbed evolution is noticed. From this combined analysis of  $\mu$ ,  $\mu^*$  and  $R_\Omega$ , we can conclude the following stages:

- (1)  $N < N_c$ ;  $\mu$  remains stable and low ( $\mu = 0.07$ ),  $\mu^*$  is very stable as well as  $R_\Omega$  after the initial drop.
- (2)  $N_c < N < 1.2 \cdot N_c$ ; After  $N_c$  ( $\mu = 0.11$ )  $R_\Omega$  is still stable but  $\mu^*$  starts to fluctuate.  $N_c$  also corresponds to the inflexion point of the coefficient of friction rising.
- (3)  $1.2 \cdot N_c < N < 1.7 \cdot N_c$ ; Continuous rising of  $\mu^*$  with significant fluctuations, continuous rising of  $\mu$  and first fluctuations of  $R_\Omega$ .
- (4)  $N > 1.7$ ; The coefficient of friction stabilizes at a second plateau around 0.4 before displaying a catastrophic increase.  $R_\Omega$  as well as  $\mu^*$  parameter displays large fluctuations indicating a severe degradation of the interface.

To better interpret the damage evolution, additional twelve tests have been duplicated and stopped at different sliding cycles. Figure 11 compares the friction evolution of these duplicated tests. A common evolution is observed displaying the four-stage response previously detailed. Dispersion is observed which, however, corresponds to the scattering generated in classical tribological tests.

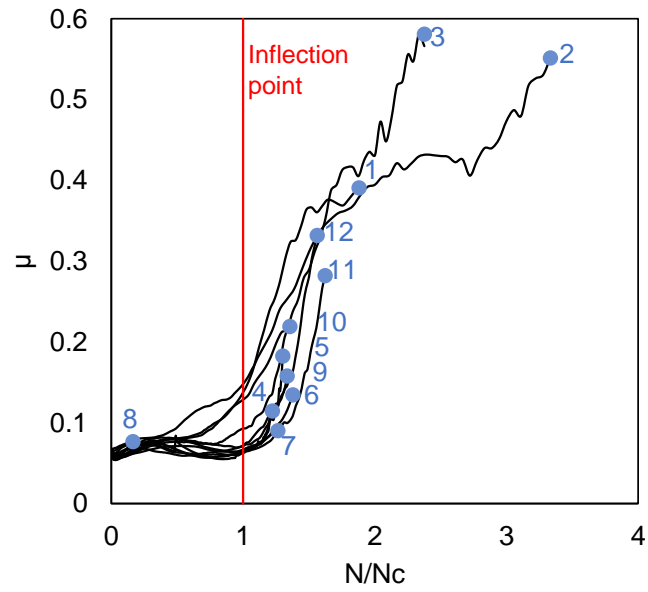


Figure 11 Normalized evolution of the tested couples (COF versus normalized cycles number,  $F_n = 40 \text{ kN}$ ,  $f = 0.2 \text{ Hz}$ ,  $\theta^* = \pm 25^\circ$ ,  $D = \pm 15 \text{ mm}$ )

Optical and 3D surface profiles have been performed on the coated and uncoated surfaces. These different analyses are compiled in Figure 12 as a function of the coefficient of friction measured at the end of each test.

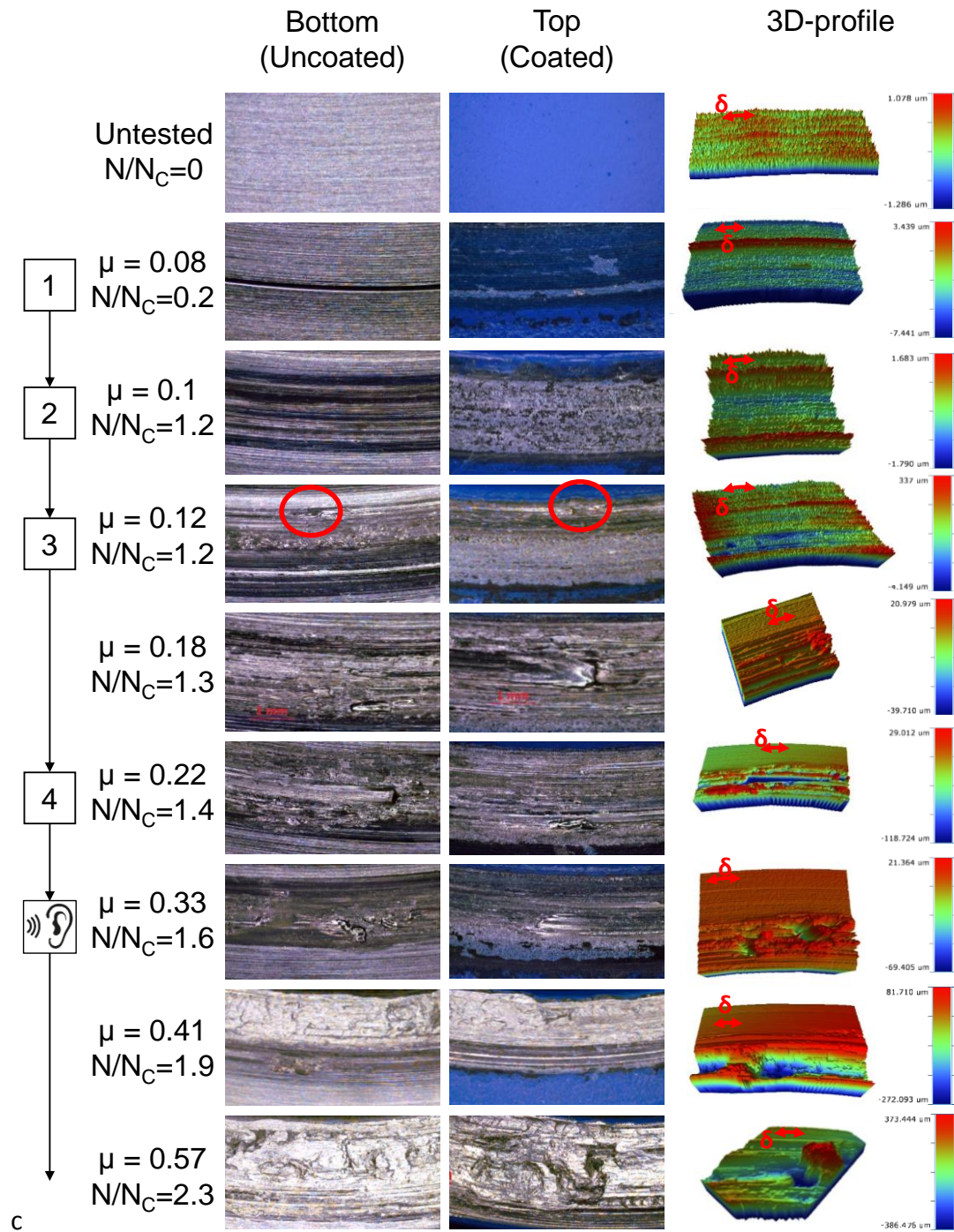


Figure 12 Evolution of the wear: optical observation and profilometry of the damage related to the studied criteria,  $F_n = 40 \text{ kN}$ ,  $f = 0.2 \text{ Hz}$ ,  $\theta^* = \pm 25^\circ$ ,  $D = \pm 15 \text{ mm}$ ,  $\bigcirc$  first adhesive spot

For  $\mu = 0.08$ , a first delamination spot of the polymer coating is observed allowing the first metal-metal contact which, as discussed previously, can explain the incipient drop of  $R_\Omega$ . For  $\mu = 0.1$ , corresponding to the first fluctuation of  $\mu^*$ , the coating is totally removed, and multiple abrasion grooves can be observed (no adhesive metal transfer is however detected). The first welded spot is observed for  $\mu = 0.12$  which also corresponds to the first disruptions on the electrical resistance  $R_\Omega$ . Then, above  $\mu = 0.12$ , adhesive wear and galling processes increase with the coefficient of friction, disruption of  $\mu^*$  and  $R_\Omega$  are observed in

domain (3). Large grooves and galling spots are already promoted, and the spot joints' size is significant (diameter of 1 mm). As the first audible acoustic emission occurs, generally related to a COF of 0.3, the surfaces appear to have experienced severe damage.

From this combined  $\mu$ ,  $\mu^*$ ,  $R_\Omega$  and surface wear observation, it can be concluded that  $N_c$ , corresponding to the friction inflexion at  $\mu = 0.1$ , can be associated to the quasi-elimination of the lubricant solid bond by abrasive wear processes. The first galling phenomenon is observed slightly after when  $\mu = 0.12$  and corresponds to first fluctuation of  $R_\Omega$ . This suggests that  $\mu^*$  appears as a pertinent parameter to detect abrasive wear processes such that  $\mu^*$  fluctuations are observed before  $\mu_c$  at the beginning of domain (2). Galling processes are actually better detected by  $R_\Omega$  fluctuations observed at the beginning of domain (3) when  $\mu = 0.12$ . This suggests that incipient galling processes may be related to a friction coefficient threshold around  $\mu_{G-onset}=0.12$  and that the pertinent parameters to detect such damage phenomenon are the fluctuations of  $R_\Omega$  (i.e. electrical contact resistance).

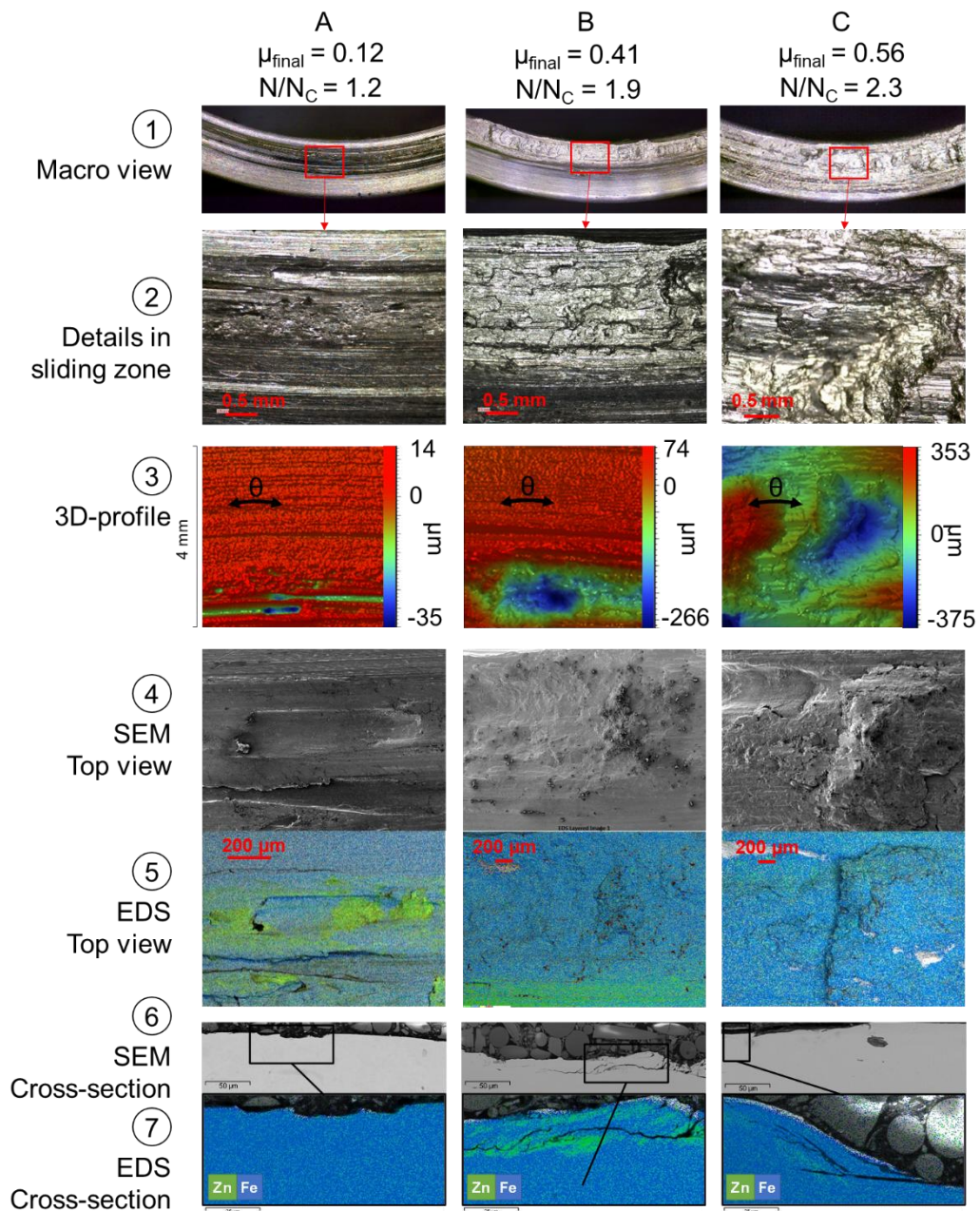


Figure 13 Surface analysis of uncoated fretted surface at  $\mu_{\text{final}}=0.12$  (A),  $\mu_{\text{final}}=0.41$  (B) and  $\mu_{\text{final}}=0.56$  (C),  $F_n = 40$  kN,  $f = 0.2$  Hz,  $\theta^* = \pm 25^\circ$ ,  $D = \pm 15$  mm



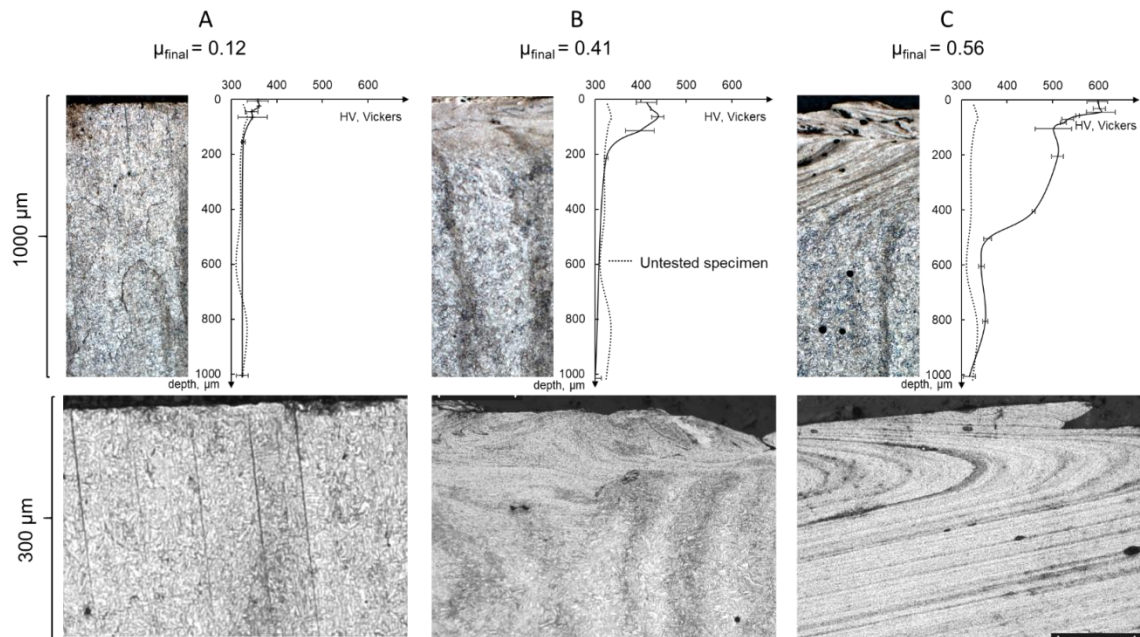


Figure 14 Subsurface (microstructural and  $\mu$ -hardness (20 mN HV)) analysis of unfretted interface at various stages of surface degradation, dotted lines account for the initial  $\mu$ -hardness profile,  $F_n = 40$  kN,  $f = 0.2$  Hz,  $\theta^* = \pm 25^\circ$ ,  $D = \pm 15$  mm

A more detailed analysis is performed at  $\mu = 0.12$  (A),  $\mu = 0.41$  (B) and  $\mu = 0.56$  (C) regarding surface damage (Figure 13) and subsurface microstructure deformation and micro-hardness evolution (Figure 14). The top view analysis shows that at  $\mu = 0.12$ , the adhesion zone is very limited (Figure 13 A-4) and most of the sliding scar rather displays an abrasion surface damage. Metal transfer is confirmed by the observation of Zn elements next to the local galling spot (Figure 13 A-5). It is also confirmed by a small lack of metal on the top surface as illustrated in Figure 13 A-6. With the surface damage extension (i.e. B,  $N/N_c = 1.9$ ,  $\mu = 0.4$ ), the adhesion zone extends displaying a significant proportion of galling area in the fretted surface (Figure 13 B-2). This is confirmed by 3D surface where a very disturbed hole can be observed (Figure 13 B-33). The adhesive wear scar, characterized by a significant mixing process of the top metal surface, is confirmed by surface (Figure 13 B-4) and cross-section (Figure 13 B-6) SEM observations. Subsurface EDS mapping confirms the mixing process (Figure 13 B-7): Zn elements coming from the coated counterpart are observed mixed with the surface steel down to  $50 \mu\text{m}$  depth below the sliding interface. At  $\mu = 0.56$ , galling damage is generalized over the whole fretted interface. The top view observation indicates a very disturbed fretted interface which was also confirmed by SEM and EDS observations. The subsurface microstructural and  $\mu$ -hardness analysis compiled in Figure 14 confirm this tendency. For  $\mu = 0.12$ , steel microstructure seems unchanged. The hardness profile is nearly equivalent to the unfretted material except on the top first  $50 \mu\text{m}$  where a slight increase of the micro-hardness ( $\pm 100$  HV) is noticed. When the friction coefficient reaches 0.4, the maximum shear stress reaches the surface [22] inducing significant plastic deformation over the first  $200 \mu\text{m}$  top layer of the surface Figure 14 B. By relating these microstructural observations with corresponding EDS mapping (Figure 14 B-7), it can be remarked that a

Mechanically Mixed Layer (MML) is detected on the top 50  $\mu\text{m}$ . Indeed, Zn elements are observed down to this depth. This is consistent with the hardness profile showing a significant growth up to maximum 450 HV at 80  $\mu\text{m}$  depth below the surface. Below this MML layer, plastic deformations are still observed until 200  $\mu\text{m}$  depth. The hardness profile suggests, however, a decrease of cumulated plastic strain since the material hardness decreases asymptotically to the reference material value (330 HV). The analysis of  $\mu = 0.56$  (C) condition underlines a severe plastic deformation up to 500  $\mu\text{m}$  below the fretted interface. No Zn element can be observed which can be explained by the fact that all the coating materials are fully removed or ejected by the wear process. The microstructural analysis confirms very severe plastic deformations with a refining process of the grain size. MML layer is suspected on the top 100  $\mu\text{m}$  characterized by very high 600 HV hardness. The transition between MML layer and the subsurface steel deformation layer is characterized by a sharp drop of the  $\mu$ -hardness from 600 to 500 HV. Then, the  $\mu$ -hardness (i.e. cumulated plastic deformation) decreases slightly to 450 HV until 400  $\mu\text{m}$  below the fretted surface. This medium 500 - 450 HV hardness corresponds well to a plastically deformed layer but cannot be attributed to the so-called TTS (Tribologically Transformed Structure). Indeed, this latter is characterized by very high hardness values (above 800 HV) and displays a very fine nano-metric grain size structure which is currently not observed in the given analysis.

This analysis suggests that the onset of galling process is very localized and does not involve significant plastic deformation within the material. However, with its extension and the associated increase of the friction coefficient, a shear plastic deformation is generated. This induces the formation of MML on thicknesses on the top 100  $\mu\text{m}$  layer below which plastic deformation of the original microstructure can be observed up to 500  $\mu\text{m}$ . In the framework of these sliding conditions, involving long sliding amplitudes ( $\pm 15$  mm), it was not possible to detect the occurrence of TTS nanostructure by contrast to usual fretting sliding conditions. This could be explained by the fact that TTS is generated and above all maintained for smaller sliding-amplitude situations.

#### 4. Discussion

From this analysis, the following tribological scenario can be concluded as detailed from steps I to V (Figure 15).

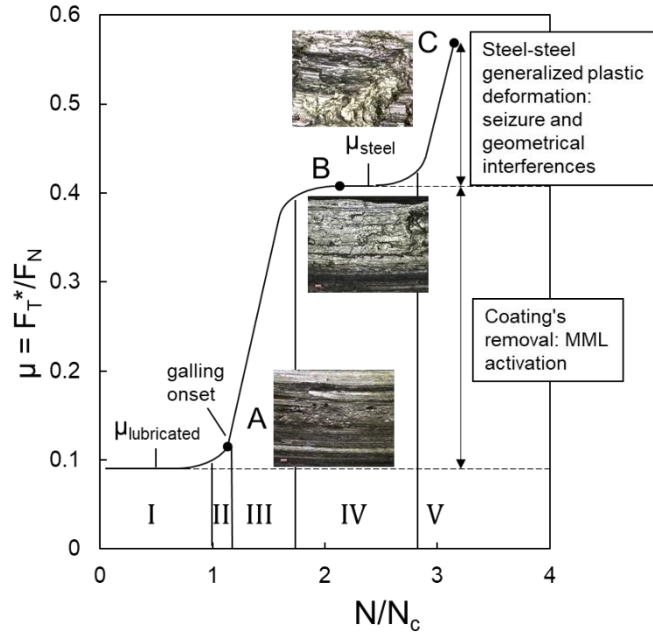


Figure 15 Illustration of the tribological scenario from solid lubricant elimination to abrasive wear, galling and global interface seizure

A first stage (I) corresponds to the progressive elimination of the solid lubricant bond until  $N_c$  when  $\mu = 0.1$ . The friction coefficient then shows a slight rising inflexion with the increase of metal interactions until the onset of adhesive wear galling process observed when  $\mu = \mu_{G-onset} = 0.12$  (II) (sliding scar A Figure 15). Then, the galled area extends over the whole interface inducing a sharp increase of the coefficient of friction (III). When all the fretted interface is covered by galling interactions, the friction coefficient stabilizes at a plateau  $\mu = 0.4$  (sliding scar B Figure 15). After this plateau, severe seizure phenomenon or geometrical interferences are suspected to sharply increase the friction coefficient up to 0.6 and even higher friction values (V). From this surface wear scenario, the evolution of the friction coefficient can be formalized as a weight function of lubricated and galling areas. Hence, the global tangential force can be described as a sum of lubricant contribution and galling contribution such that:

$$F_t = F_{tL} + F_{tG} \quad (5)$$

$$\text{with } F_{tL} = A_L \cdot \mu_L \cdot p_{mean} \quad (6)$$

the contribution of lubricant

$$\text{and } F_{tG} = A_G \cdot \mu_G \cdot p_{mean} \quad (7)$$

the contribution of galling

where  $A_L$  and  $A_G$  are related to lubricated and galled areas respectively and  $\mu_L$  and  $\mu_G$  the friction coefficient for pure lubricated or galled interfaces. By defining  $F_n = A \cdot p_{mean}$  where  $A = A_L + A_G$  is the total contact area, an analysis in terms of friction coefficient can be developed as follows:

$$\mu = \frac{F_t}{F_n} = \frac{A_L \cdot \mu_L \cdot p_{mean} + A_G \cdot \mu_G \cdot p_{mean}}{A \cdot p_{mean}} \quad (8)$$

$$\mu = \mu_L + \frac{A_G}{A} \cdot (\mu_G - \mu_L) \quad (9)$$

Knowing  $\mu_L$  and  $\mu_G$ , the evolution of  $\mu$  is simply dependent on the relative evolution of the galling area compared to the contact area (i.e.  $A_G/A$  function). Former fretting wear investigations suggest that the dynamical degradation of a solid lubricant bond can be expressed as a function of the accumulated Archard work dissipated within the interface such that:

$$\Sigma\omega = 4 \cdot N \cdot p_{mean} \cdot \delta^* \quad (10)$$

Figure 16 compares the various friction curves versus the normalized  $\Sigma\omega/\Sigma\omega_c$  parameter.

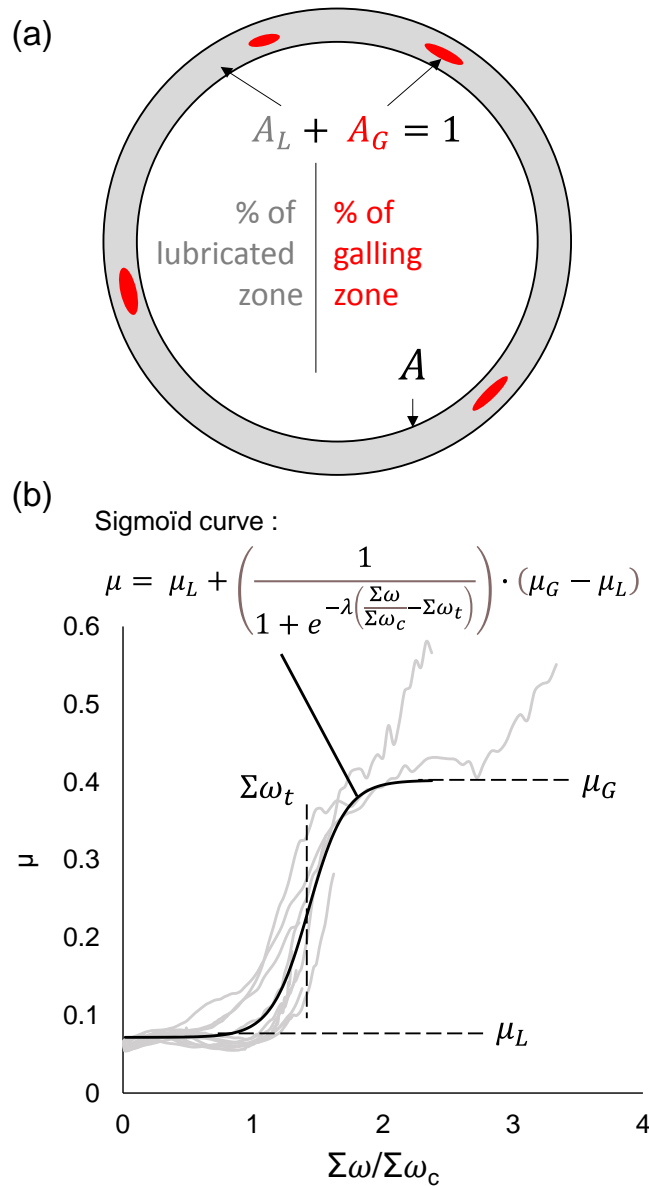


Figure 16 (a) Illustration of the evolution of the partition between lubricated and galling fretted area, (b) evolution of  $\mu$  versus  $\Sigma\omega/\Sigma\omega_c$

The global evolution of friction curve can be fitted using a simple sigmoid function:

$$\mu = \mu_L + \left( \frac{1}{1 + e^{-\lambda \left( \frac{\Sigma\omega}{\Sigma\omega_c} - \Sigma\omega_t \right)}} \right) \cdot (\mu_G - \mu_L) \quad (11)$$

with  $\mu_L = 0.074$ ,  $\mu_G = 0.42$ ,  $\Sigma\omega_t = 1.46$  and  $\lambda = 7$ . A very good correlation is indeed observed with the experiments. Besides, by comparing equations (9) and (11), the relative partition of galling areas can be identified assuming a galling area ratio  $\%A_G$ :

$$\%A_G = \frac{A_G}{A} = \frac{1}{1 + e^{-\lambda \left( \frac{\Sigma\omega}{\Sigma\omega_c} - \Sigma\omega_t \right)}} \quad (12)$$

Hence, using a limited number of variables ( $\mu_L$ ,  $\mu_G$ ,  $\Sigma\omega_t$ ,  $\lambda$ ), it is possible to depict the friction behavior for pure lubricated conditions to pure galling response. To ensure that this model gives a valid description of galled area evolution at the surface, measurements on optical observation were made.

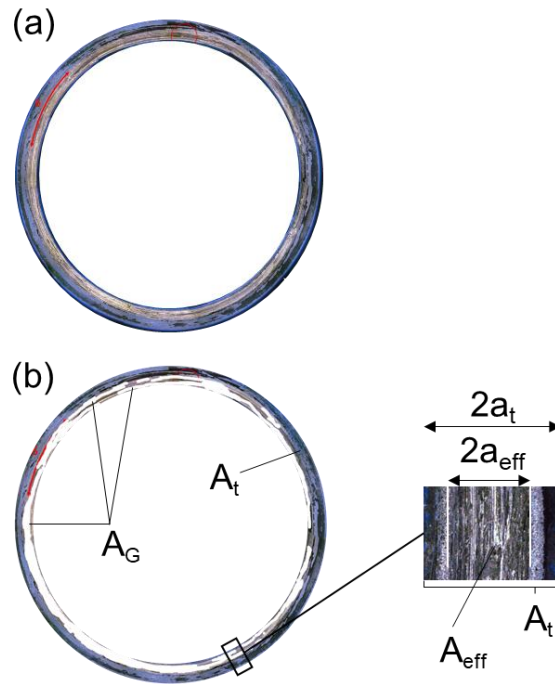


Figure 17 (a) Original picture, (b) image analysis to establish the experimental galling area

Measurements have been done using image analysis of the whole fretted surface showing that galling areas were spotted with white pixels (Figure 17). The white area (i.e. sum of the white pixels observed in the fretted area) is assumed representative of the galling area  $A_G$ . The proportion of the galling area can be therefore estimated as:

$$\%A_{G,exp} = \frac{A_G}{A_t} \quad (13)$$

where  $A_t$  is the total fretted area:

$$A_t = L \cdot 2a_t \quad (14)$$

with  $L$  the mean perimeter and  $a_t$  the contact half-width of the fretted area. This experimental value is compared versus the theoretical estimation extracted from the friction behavior analysis (Figure 18a). Another good correlation is observed. The measured value  $\%A_{G,exp}$  value is, however, systematically lower than the predicted one. This can be explained examining more carefully the fretted interface. Galling areas are systematically observed in the median part of the fretted area. No galling areas are observed on the lateral sides. Indeed, due to the toric shape of the upper specimen, the contact extends with the surface wear. Hence, the lateral border endures a lower friction work than in the inner part of the contact. One strategy to palliate this effect consists in assuming an inner “effective” fretted interface where galling can occur so that:

$$A_{eff} = 2 \cdot a_{eff} \cdot L \approx \beta \cdot A_t \quad (15)$$

Various observations suggest that  $A_{eff}$  can be approximated as a  $\beta$  proportion of the total area with  $\beta \approx 0.8$ . An effective galling area ratio can therefore be estimated so that:

$$\%A_{G,eff} = \frac{A_G}{A_{eff}} = \frac{A_G}{\beta \cdot A_t} \quad (16)$$

Figure 18b compares the  $\%A_{G,th}$  versus the effective experimental value  $\%A_{G,eff}$ . A better correlation is observed which indirectly supports the proposal. However, this approach could be improved by considering a variable evolution of the  $\beta$  coefficient with the surface wear extension. This unfortunately cannot be addressed in the frame of this investigation. However, developments will consist in investigating flat-on-flat interface limiting the discrepancy induced by surface wear extension.

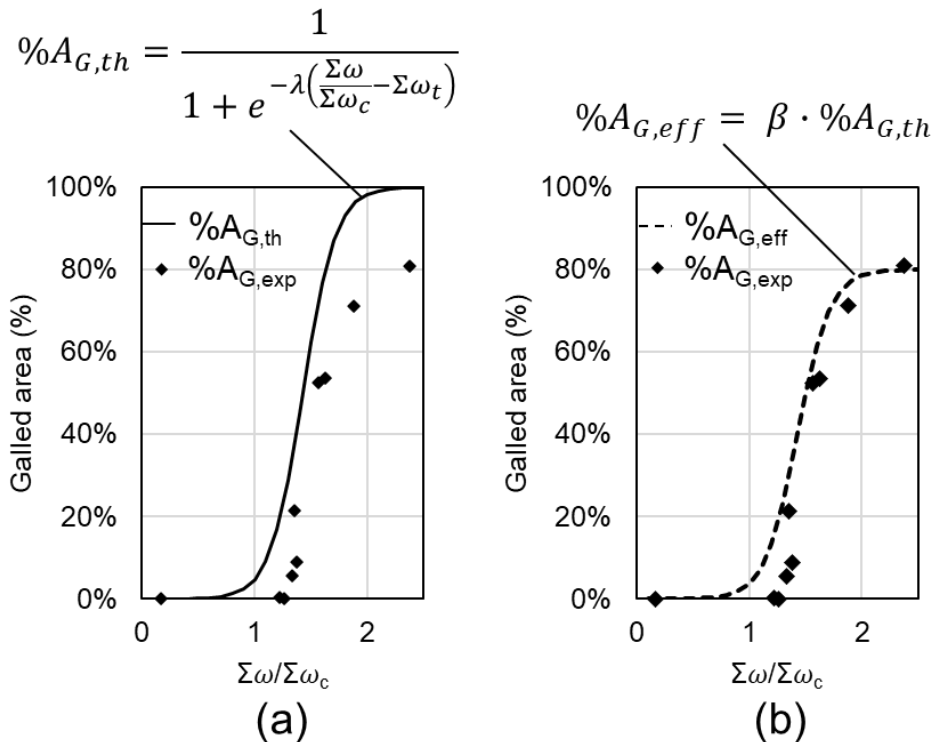


Figure 18 (a) Comparison between theoretical and nominal galling area ratio, (b) comparison between theoretical and effective galling area ratio

This model is, however, not able to compare the final seizure damage which necessitates developing a specific physical analysis of such very complex phenomena.

## 5. Conclusion

The purpose of this research is to investigate and quantify the galling occurrence and the related damage of a solid lubricant steel-steel interface subjected to severe sliding conditions. The following points emerge from this experimental investigation:

- An original ring-on-ring sliding test equivalent to the ASTM G196 norm was developed to investigate macro-contacts. Using this set up, it is possible to test real industrial oil and gas steel tubing.
- This tribological test was instrumented to follow the evolution of the friction coefficient ( $\mu$ ), the friction noise during the sliding sequence ( $\mu^*$ ) and the electrical contact resistance ( $R_\Omega$ ).
- A solid lubricant steel-steel interface was investigated. A five-step tribological wear scenario was depicted from the progressive elimination of the lubricated bond, the abrasive wear, the onset of galling, the galling extension and finally the global seizure of the interface. The  $R_w$  ECR parameter and the related fluctuations appear as the most promising strategy to detect the onset of galling phenomenon. That onset of galling phenomenon was related to a rather low threshold  $\mu_{G-onset} = 0.12$  friction value (at least for the studied interfaces). With the galling extension and the related rising of the interface shear, severe plastic deformation as well as MML debris layers are generated. However, no TTS structure could be observed which is attributed to the large sliding amplitudes imposed resulting in easier TTS ejection from the interface.
- A simple sigmoid formulation of the relative extension of the galling area was proposed to fit the evolution of the global friction coefficient through a basic "Dalton law", summing the shear contribution induced by the lubricated and the galled areas.
- From the friction analysis a theoretical galling area ratio (i.e.  $\%A_G = A_G/A_t$ ) was derived and compared versus experiments. A good correlation was observed which can be improved by replacing the nominal fretted area  $A_t$  by the inner effective fretted area  $A_{eff}$  where surface wear can effectively promote galling processes.

Future development will try to formalize the galling endurance varying the loading conditions as well as investigating new steel alloys and lubricants. More fundamental research will be also performed to characterize the micro-mechanical properties of the galling spot and the related plastically deformed materials. Finally, a flat-on-flat contact configuration will be preferred to avoid the discrepancy induced by the continuous contact area extension related to hertzian contact configuration.

## 6. References

- [1] W.R. Blackstone, The development of a new test method for the evaluation of galling in OCTG connections, Thesis, Texas Tech University, 1987. <https://ttu-ir.tdl.org/handle/2346/12310> (accessed April 19, 2021).
- [2] C. Blanc, J. Lewis, A. Ichim, D. Mutis, A. Zestran, C.I. Lucca, L. Perello, New OCTG Developments to Overcome Challenges in Unconventional Plays, in: Day 2 Wed, October 16, 2019, SPE, Charleston, West Virginia, USA, 2019: p. D021S001R002. <https://doi.org/10.2118/196596-MS>.
- [3] O.G. Meza, S.. Sinaga, Overview of Lubrication Regimes and Contact Pressure Distribution in Proprietary Tubular Connections for Special Drilling Environments, in: Day 1 Mon, January 29, 2018, SPE, Abu Dhabi, UAE, 2018: p. D011S004R004. <https://doi.org/10.2118/189367-MS>.
- [4] J.L. Bishop, C.M.McC. Ettles, The seizure of journal bearings by thermoelastic mechanisms, *Wear*. 79 (1982) 37–52. [https://doi.org/10.1016/0043-1648\(82\)90202-2](https://doi.org/10.1016/0043-1648(82)90202-2).
- [5] E.F. Finkin, Adhesive wear: a general review of the state of experimental knowledge and theory, *International Journal of Materials in Engineering Applications*. 1 (1979) 154–161. [https://doi.org/10.1016/0141-5530\(79\)90004-9](https://doi.org/10.1016/0141-5530(79)90004-9).
- [6] P.A. Swanson, L.K. Ives, E.P. Whinton, M.B. Peterson, A study of the galling of two steels using two test methods, *Wear*. 122 (1988) 207–223. [https://doi.org/10.1016/0043-1648\(88\)90078-6](https://doi.org/10.1016/0043-1648(88)90078-6).
- [7] F.W. Lindvall, On tool steel, surface preparation, contact geometry and wear in sheet metal forming, (n.d.) 57.
- [8] S. Baydoun, S. Fouvry, An experimental investigation of adhesive wear extension in fretting interface: Application of the contact oxygenation concept, *Tribology International*. 147 (2020) 106266. <https://doi.org/10.1016/j.triboint.2020.106266>.
- [9] J. Juoksukangas, V. Nurmi, J. Hintikka, M. Vippola, A. Lehtovaara, A. Mäntylä, J. Vaara, T. Frondelius, Characterization of cracks formed in large flat-on-flat fretting contact, *International Journal of Fatigue*. 124 (2019) 361–370. <https://doi.org/10.1016/j.ijfatigue.2019.03.004>.
- [10] P. Arnaud, S. Baydoun, S. Fouvry, Modeling adhesive and abrasive wear phenomena in fretting interfaces: A multiphysics approach coupling friction energy, third body and contact oxygenation concepts, *Tribology International*. 161 (2021) 107077. <https://doi.org/10.1016/j.triboint.2021.107077>.
- [11] S. Fouvry, C. Paulin, An effective friction energy density approach to predict solid lubricant friction endurance: Application to fretting wear, *Wear*. 319 (2014) 211–226. <https://doi.org/10.1016/j.wear.2014.07.009>.
- [12] G02 Committee, Test Method for Galling Resistance of Material Couples, ASTM International, 2008. <https://doi.org/10.1520/G0196-08R16>.
- [13] K.K. Kakulite, B. Kandasubramanian, Rudiment of ‘galling: Tribological phenomenon’ for engineering components in aggregate with the advancement in functioning of the anti-galling coatings, *Surfaces and Interfaces*. 17 (2019) 100383. <https://doi.org/10.1016/j.surfin.2019.100383>.
- [14] E. Rabinowicz, Friction seizure and galling seizure, *Wear*. 25 (1973) 357–363. [https://doi.org/10.1016/0043-1648\(73\)90006-9](https://doi.org/10.1016/0043-1648(73)90006-9).
- [15] V. Nurmi, J. Hintikka, J. Juoksukangas, M. Honkanen, M. Vippola, A. Lehtovaara, A. Mäntylä, J. Vaara, T. Frondelius, The formation and characterization of fretting-induced degradation layers using quenched and tempered steel, *Tribology International*. 131 (2019) 258–267. <https://doi.org/10.1016/j.triboint.2018.09.012>.



- [16] S.R. Hummel, J. Helm, Gallings50, a Stochastic Measure of Galling Resistance, *Journal of Tribology*. 131 (2009). <https://doi.org/10.1115/1.3123344>.
- [17] A. Ertas, H.J. Carper, O. Cuvalci, S. Ekwaro-Osire, W.R. Blackstone, Experimental Investigation of Galling Resistance in OCTG Connections, *Journal of Engineering for Industry*. 114 (1992) 100–104. <https://doi.org/10.1115/1.2899745>.
- [18] H.J. Carper, A. Ertas, J. Issa, O. Cuvalci, Effect of Some Material, Manufacturing, and Operating Variables on the Friction Coefficient in OCTG Connections, *Journal of Tribology*. 114 (1992) 698–705. <https://doi.org/10.1115/1.2920938>.
- [19] O. Cuvalci, H. Sofuoglu, A. Ertas, Effect of surface coating and tin plating on friction characteristics of P-110 tubing for different thread compounds, *Tribology International*. 36 (2003) 757–764. [https://doi.org/10.1016/S0301-679X\(03\)00057-4](https://doi.org/10.1016/S0301-679X(03)00057-4).
- [20] API Specification 5CT, Casing and tubing, API, 2021. <https://www.api.org/>.
- [21] T. Galle, W. De Waele, D.B. Patrick, J. Van Wittenberghe, Influence of design features on the structural integrity of threaded pipe connections, *IJSMED*. 2 (2011) 237–245. <https://doi.org/10.21825/scad.v2i2.20521>.
- [22] K.L. Johnson, K.L. Johnson, *Contact Mechanics*, Cambridge University Press, 1987.